

## Article

# In Situ Crosslinked Biodegradable Hydrogels Based on Poly(Ethylene Glycol) and Poly( $\epsilon$ -Lysine) for Medical Application

Xia Ding<sup>1</sup>, Bing Yang<sup>1,\*</sup> and Zhaosheng Hou<sup>2,\*</sup> <sup>1</sup> School of Intelligence Engineering, Shandong Management University, Jinan 250357, China; 14438120160212@sdu.edu.cn<sup>2</sup> College of Chemistry, Chemical Engineering and Materials Science, Shandong Normal University, Jinan 250014, China

\* Correspondence: 14438120160171@sdu.edu.cn (B.Y.); houzs@sdu.edu.cn (Z.H.)

**Abstract:** Hydrogels have emerged as promising biomaterials due to their excellent performance; however, their biocompatibility, biodegradability, and absorbability still require improvement to support a broader range of medical applications. This paper presents a new biofunctionalized hydrogel based on in situ crosslinking between maleimide-terminated four-arm-poly(ethylene glycol) (4-arm-PEG-Mal) and poly( $\epsilon$ -lysine) ( $\epsilon$ -PL). The PEG/ $\epsilon$ -PL hydrogels, named LG-n, were rapidly formed via amine/maleimide reaction by mixing 4-arm-PEG-Mal and  $\epsilon$ -PL under physiological conditions. The corresponding dry gels (DLG-n) were obtained through a freeze-drying technique. <sup>1</sup>H NMR, FT-IR, and SEM were utilized to confirm the structures of 4-arm-PEG-Mal and LG-n (or DLG-n), and the effects of solid content on the physicochemical properties of the hydrogels were investigated. Although high solid content could increase the swelling ratio, all LG-n samples exhibited a low equilibrium swelling ratio of less than 30%. LG-7, which contained moderate solid content, exhibited optimal compression properties characterized by a compressive fracture strength of 45.2 kPa and a deformation of 69.5%. Compression cycle tests revealed that LG-n demonstrated good anti-fatigue performance. In vitro degradation studies confirmed the biodegradability of LG-n, with the degradation rate primarily governing the drug (ceftibuten) release efficiency, leading to a sustained release duration of four weeks. Cytotoxicity tests, cell survival morphology observation, live/dead assays, and hemolysis tests indicated that LG-n exhibited excellent cytocompatibility and low hemolysis rates (<5%). Furthermore, the broad-spectrum antibacterial activity of LG-n was verified by an inhibition zone method. In conclusion, the developed LG-n hydrogels hold promising applications in the medical field, particularly as drug sustained-release carriers and wound dressings.



**Citation:** Ding, X.; Yang, B.; Hou, Z. In Situ Crosslinked Biodegradable Hydrogels Based on Poly(Ethylene Glycol) and Poly( $\epsilon$ -Lysine) for Medical Application. *Molecules* **2024**, *29*, 5435. <https://doi.org/10.3390/molecules29225435>

Academic Editors: Fei Song and Li-Ming Zhang

Received: 14 October 2024

Revised: 15 November 2024

Accepted: 16 November 2024

Published: 18 November 2024



**Copyright:** © 2024 by the authors. Licensee MDPI, Basel, Switzerland. This article is an open access article distributed under the terms and conditions of the Creative Commons Attribution (CC BY) license (<https://creativecommons.org/licenses/by/4.0/>).

## 1. Introduction

Hydrogels are three-dimensional networks of hydrophilic polymers that have high water-retaining capabilities [1,2]. They can maintain structural integrity while swelling in aqueous medium or physiological fluids. The flexibility, tunable mechanical properties, and favorable biocompatibility make them ideal for various medical applications, including drug delivery [3,4], cell culture [5], tissue engineering [6–8], and wound healing [9,10]. In recent years, smart hydrogels with external triggers (temperature, electricity, magnetism, pH, light, etc.) have been developed for targeted-release drug delivery systems, which can effectively reduce the side effects of drugs [11–13]. Many strategies are explored to prepare hydrogels, including chemical reactions, and light- and heat-induced polymerization reactions [14,15]. However, these approaches have drawbacks, including potential toxicity, delayed gelation, or requiring supplementary devices [16]. Moreover, most of the produced hydrogels exhibit instability and a concurrent loss of bioactivity due to their uncontrolled

gelation chemistries [17,18]. Therefore, developing a simple and rapid method to prepare biodegradable hydrogels with high biocompatibility and biostability is significant for broadening their applications in the medical field.

Poly(ethylene glycol) (PEG) is a versatile nonionic polymer known for its high biocompatibility, superior hydrophilicity, and non-toxicity [19]. The adjustment of its molecular weight and structure enables tailored applications in various pharmaceutical and medical areas, such as in drug delivery systems to enhance solubility and bioavailability, in tissue engineering as scaffolds for cell growth, and in oncology through PEGylation to reduce immunogenicity [20–22]. PEG-based hydrogels exhibited exceptional efficacy in guiding the behavior of encapsulated cells due to their inherent resistance to protein adsorption [23,24]. Recently, hydrogel systems made from multi-arm PEGs or their derivatives have been designed as promising scaffolds for applications in tissue engineering [25,26].

$\epsilon$ -Poly(L-lysine) ( $\epsilon$ -PL), a natural cationic antibacterial peptide, is composed of  $\epsilon$ -lysine by isopeptide bonds [27,28]. This compound exhibited various beneficial properties, including biocompatibility, biodegradability, water solubility, thermal stability, edibility, and antibacterial effects [29,30]. The body can rapidly metabolize  $\epsilon$ -PL through its enzyme system into the monomer  $\epsilon$ -lysine, which is subsequently absorbed, thereby minimizing the potential for accumulation and toxicity. Furthermore, the antibacterial characteristics of  $\epsilon$ -PL effectively inhibit the growth and reproduction of various microorganisms, which reduces the risk of infection and improves the safety of medical devices [31,32]. Consequently,  $\epsilon$ -PL presents a promising biomedical material for various applications, such as antibacterial surface coatings, drug delivery systems, and protective films [33–35]. However, the polycationic nature of  $\epsilon$ -PL can lead to non-specific interactions with cell membranes, potentially impacting drug targeting [36]. Additionally, its relatively rapid degradation rate could influence the effectiveness of long-term drug release.

In this paper, *in situ* crosslinked hydrogels were developed through the amine/maleimide reaction between maleimide-terminated four-arm-poly(ethylene glycol) (4-arm-PEG-Mal) and  $\epsilon$ -PL under physiological conditions for medical application. 4-Arm-PEG-Mal was first synthesized from a commercially available 4-arm-PEG-OH. Subsequently, PBS solutions of 4-arm-PEG-Mal and  $\epsilon$ -PL were mixed and sprayed using a double-barrel syringe to rapidly produce hydrogels with varying solid content. The corresponding dry gels were obtained through freeze drying. The effect of the solid content in hydrogels on their physicochemical characteristics (thermal properties, mechanical properties, swelling behavior, degradation performance, and drug release properties) was investigated. The biocompatibility of the hydrogels was preliminarily evaluated through cytotoxicity tests, cell survival morphology observation, live/dead assays, and hemolysis tests. Additionally, the antibacterial properties of the hydrogels were assessed using the inhibition zone method.

## 2. Results and Discussion

### 2.1. Preparation of LG-n Hydrogels

Due to the electrophilicity of 4-arm-PEG-Mal and nucleophilicity of  $\epsilon$ -PL, the electrophilic-nucleophilic substitution reactions easily occurred under mild conditions by mixing their solution at different pH values, resulting in the formation of crosslinked PEG/ $\epsilon$ -PL hydrogels (LG-n). Direct mixing of the two solutions yielded an inconsistent mixture, which compromised the hydrogel formation process. To address this, a double syringe equipped with a helical mixing head (Figure 1) was adopted to facilitate complete reactions between the two components, thereby promoting the formation of a homogeneous hydrogel. It provided a more controlled, efficient, and scalable method for hydrogel formation compared to direct mixing methods. After the 15 s of spraying, the mixture exhibited negligible flow, and by 40 s, the hydrogel had formed essentially.

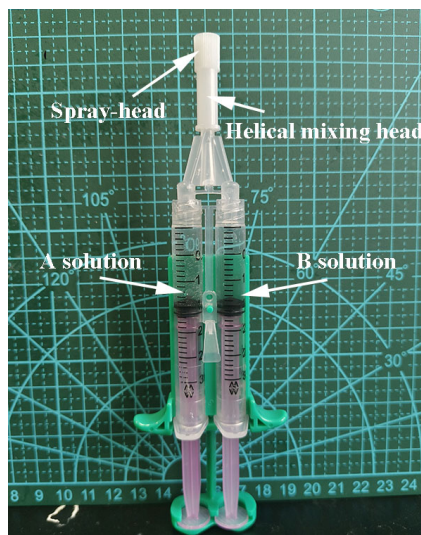


**Figure 1.** Photo of the dual-chamber syringe equipped with a helical mixing head.

## 2.2. FT-IR Spectra

The chemical structures of  $\varepsilon$ -PL, 4-arm-PEG-Mal, and dry PEG/ $\varepsilon$ -PL gels (DLG-n) were characterized by FT-IR, and the spectra are displayed in Figure 2 (DLG-n samples have similar FT-IR spectra, and DLG-7 is taken as a representative sample). In the FT-IR spectrum of  $\varepsilon$ -PL (Figure 2a), the absorption peaks at 3233, 2930, 1663, 1551, 1250, and 508  $\text{cm}^{-1}$  belonged to the stretching vibrations of N-H, C-H, amide I, amide II, C-N, and  $-\text{NH}_2$ , respectively. In addition, a broad strong absorption was observed at 3000~2800  $\text{cm}^{-1}$ , which was attributed to the asymmetric and symmetric stretching vibrations of  $-\text{NH}_3^+$  [37]. 4-arm-PEG-Mal (Figure 2b) exhibited the characteristic absorption of  $-\text{CH}_2-$ , ester C=O, and ether C—O—C at 2870, 1735, and 1090  $\text{cm}^{-1}$ , respectively. The weak peaks at 1774 and 1806  $\text{cm}^{-1}$  were ascribed to the characteristic absorption of the C=O and amide groups in the maleimide ring. The maleimide groups were linked only at the end of the PEG chain, and their low content resulted in reduced absorption intensity, proving the successful synthesis of 4-arm-PEG-Mal. In the FT-IR spectrum of DLG-7 (Figure 2c), the characteristic peaks of  $\varepsilon$ -PL and 4-arm-PEG-Mal were observed. The absorption peaks of  $-\text{CH}_2-$ , ester C=O, amide I, amide II, ether C—O—C, and  $-\text{NH}_2$  appeared at 2875, 1716, 1650, 1548, 1090, and 508  $\text{cm}^{-1}$ , respectively. The absorption intensity of  $-\text{NH}_3^+$  (3000~2900  $\text{cm}^{-1}$ ) showed a significant decrease, accompanied by a broader band of amide (508  $\text{cm}^{-1}$ ), which confirmed that the chemical reactions of maleimide/ $-\text{NH}_2$  indeed occurred and the cross-linked structures were formed. It was worth noting that the absorption peaks for ester C=O and amide I exhibited a blue shift, due to the H-bonds formed between C=O and  $-\text{NH}_2$ . A similar phenomenon was also observed in our reported poly(ether-urethane) elastomers based on phenol-urethane bonds [38]. Additionally, the broad peak at 3351  $\text{cm}^{-1}$  corresponded to the absorption of residual moisture in the dry gel.

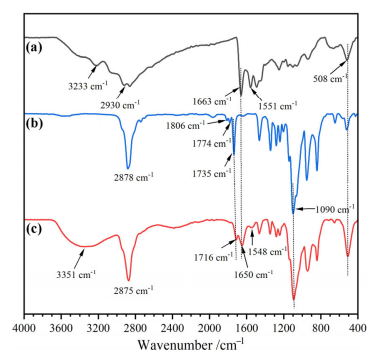


**Figure 2.** FT-IR spectra for (a)  $\varepsilon$ -PL, (b) 4-arm-PEG-Mal, and (c) DLG-7.

### 2.3. Microstructure

The SEM images of DLG-n with various solid content are presented in Figure 3. A porous structure with significant interconnectivity was observed across all samples [39]. Twenty pores were selected from each SEM image to measure the pore sizes (Photoshop CS6<sup>TM</sup>) and pore size distribution (Origin 2020<sup>TM</sup>). The average pore sizes were  $498 \pm 71$ ,  $454 \pm 65$ , and  $394 \pm 59 \mu\text{m}$  for DLG-3, -7, and -11, respectively. The pore size gradually decreased with the increase in solid content in the hydrogels, which correspondingly indicated a reduction in the density of the samples. The dense pores enhanced the contact surface between the dry gel and water molecules, thereby facilitating water retention in the hydrogel. Furthermore, this structure effectively dispersed the external forces, thus preserving the shape of the hydrogels and enhancing their anti-compressive properties [40]. The porous network structure contributed to excellent water absorbency and favorable mechanical properties.

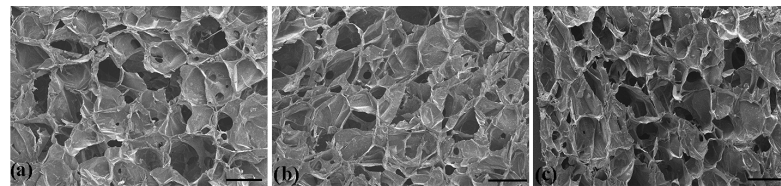


**Figure 3.** SEM photos of (a) DLG-3, (b) DLG-7, (c) DLG-11 (scale bar: 500  $\mu\text{m}$ ).

### 2.4. TGA Analysis

Figure 4 shows the TGA and DTG curves of  $\epsilon$ -PL, 4-arm-PEG-Mal, and DLG-n, and the characteristic values derived from the curves are listed in Table 1. The pyrolysis process of  $\epsilon$ -PL could be divided into two weight-loss stages, which was consistent with the reported result [41]. The first stage occurred at low temperatures with a maximum temperature ( $T_1$ ) of 315.0 °C belonged to the thermal decomposition of the amide bond in the main chain. The slight weight loss in the second stage with  $T_2$  of 449.6 °C originated from the decomposition of the organic salt in the side chain. The heat-resistant organic salts resulted in a residual weight ( $W_r$ ) of up to 14.6% at the end of the test. A two-step weight loss was found in the thermal decomposition curves of 4-arm-PEG-Mal. The slight mass loss at 306.0 °C ( $T_1$ ) was attributed to the pyrolysis of ester bonds, and the main mass loss at 405.6 °C ( $T_2$ ) belonged to the decomposition of ether bonds in the backbone [42]. DLG-n with different solid content exhibited overlapped TGA curves, meaning similar thermal stability. It could be concluded that the solid content had little effect on the thermal stability of the dry gel. Only one weight-loss peak with  $T_2$  ranging from 411.2 to 421.0 °C was found in the DTG curves of DLG-n, manifesting good component compatibility. The  $T_{5\%}$  of DLG-n appeared at ~370 °C, which was much higher than that of  $\epsilon$ -PL (289.3 °C) and 4-arm-PEG-Mal (295.4 °C). The high initial thermal stability of DLG-n should be ascribed to the three-dimensional network structure linked by covalent amide bonds and noncovalent H-bonds, which needed more energy to decompose. It indicated that crosslinking improved the heat resistance of DLG-n and a  $T_{5\%}$  higher than 200 °C meant that the dry gels were suitable for high-temperature sterilization.

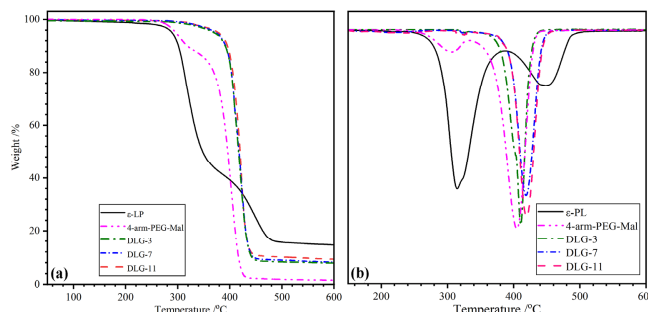


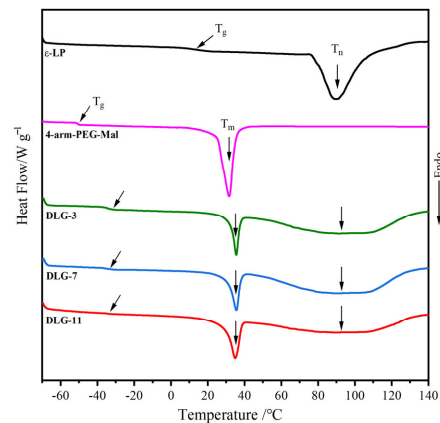
**Figure 4.** (a) TGA and (b) DTG curves of  $\epsilon$ -PL, 4-arm-PEG-Mal, and DLG-n.

**Table 1.** Characteristic values of  $\varepsilon$ -PL, 4-arm-PEG-Mal, and DLG-n from TGA and DTG curves.

Samples	$T_{5\%}/^{\circ}\text{C}$	$T_1/^{\circ}\text{C}$	$T_2/^{\circ}\text{C}$	$W_r/\%$
$\varepsilon$ -PL	289.3	315.0	449.6	14.6
4-arm-PEG-Mal	295.4	306.1	405.6	1.6
DLG-3	377.8	/	411.2	8.2
DLG-7	371.8	/	418.6	7.9
DLG-11	370.3	/	421.1	7.8

### 2.5. DSC Analysis

The DSC curves for  $\varepsilon$ -PL, 4-arm-PEG-Mal, and DLG-n are presented in Figure 5, and the thermal transition values are summarized in Table 2.  $\varepsilon$ -PL exhibited a slightly higher glass transition temperature ( $T_g$ ) at  $13.4\ ^{\circ}\text{C}$ , which was due to the  $\text{NH}_3^+$  in the side chain. As reported in the published paper, the  $T_g$  of 4-arm-PEG-Mal appeared at a low temperature of  $-50\ ^{\circ}\text{C}$ , owing to its highly flexible ether bonds [43]. Only one  $T_g$  was observed in the crosslinked DLG-n curves, indicating good compatibility between PEG and  $\varepsilon$ -PL. The crosslinked network structure reduced the flexibility of the ether bonds, resulting in higher  $T_g$  values than 4-arm-PEG-Mal. The  $T_g$  values of approximately  $\sim -34\ ^{\circ}\text{C}$  meant that DLG-n chains were in a highly flexible state at normal temperature, which was a crucial factor for enabling the mechanical properties of the hydrogels. In addition, both  $\varepsilon$ -PL and 4-arm-PEG-Mal displayed a distinct crystal melting endothermic peak, appearing at  $76\text{--}110\ ^{\circ}\text{C}$  ( $T_m = 89.3\ ^{\circ}\text{C}$ ,  $\Delta H_m = 43.9\ \text{J}\cdot\text{g}^{-1}$ ) and  $24\text{--}37\ ^{\circ}\text{C}$  ( $T_m = 31.7\ ^{\circ}\text{C}$ ,  $\Delta H_m = 28.1\ \text{J}\cdot\text{g}^{-1}$ ), respectively. Both endothermic peaks appeared in the DSC curves of DLG-n; however, the corresponding  $\Delta H$  values were significantly lower than those of the raw materials. This reduction could be attributed to the crosslinking, which hindered the orderly arrangement of chains and decreased crystallization capacity. The similar DSC curves of DLG-n demonstrated that the solid content did not affect their thermal transition properties.

**Figure 5.** DSC curves of  $\varepsilon$ -PL, 4-arm-PEG-Mal, and DLG-n.**Table 2.** Characteristic values of  $\varepsilon$ -PL, 4-arm-PEG-Mal, and DLG-n from DSC curves.

Samples	$T_g/^{\circ}\text{C}$	$T_m/^{\circ}\text{C}$	$T_n$	$\Delta H_m/\text{J}\cdot\text{g}^{-1}$	$\Delta H_n/\text{J}\cdot\text{g}^{-1}$
$\varepsilon$ -PL	13.4	—	89.3	—	43.9
4-arm-PEG-Mal	-49.6	31.7	—	28.1	—
LG-3	-33.9	45.6	97.1	15.2	25.2
LG-7	-33.9	45.6	97.4	14.7	26.2
LG-11	-33.8	45.5	96.9	14.6	25.9

## 2.6. Swelling Performance

Swelling studies were conducted to investigate the influence of solid content on the performance of the prepared hydrogels. The swelling behaviors of the LG-n with different solid contents were explored over time, and the resulting swelling curves are presented in Figure 6. All samples exhibited a rapid initial increase in SR, followed by gradually slowing down and achieving equilibrium. The time required for LG-3, -7, and -11 samples to reach swelling equilibrium was 25, 50, and 70 min, respectively. The corresponding equilibrium swelling rates (ESRs) for these samples were 11.8%, 16.5%, and 26.4%. The results indicated that with an increase in solid content in hydrogels, both the SR and ESR exhibited a significant rise. This phenomenon can be attributed to two primary factors [44]: one is the hydrophilicity of the PEG segment, which increases with the rising solid content; another is the tighter network structure formed by the higher solid content. Consequently, high solid content could enhance the water-holding capacity of the hydrogel, resulting in a slower SR and a higher ESR. It should be noted that LG-n hydrogels with different solid content presented low swelling properties with ESR values less than 30%.

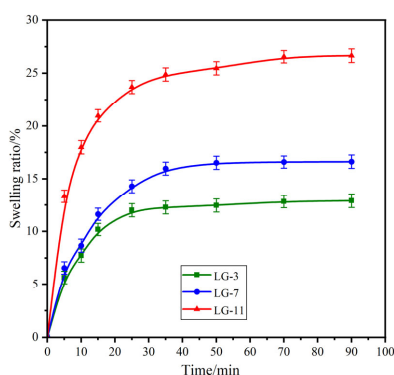


**Figure 6.** Swelling curves of  $\epsilon$ -PL, 4-arm-PEG-Mal, and DLG-n ( $n = 3$ ).

## 2.7. Compression Performance

The compressive performance of hydrogels is of paramount importance, as it dictates their capacity to withstand external stress and maintain structural integrity in practical applications. The compressive stress–strain profiles of the covalently crosslinked LG-n are expressed in Figure 7a. As expected, the compressive strength ( $\sigma$ ) increased with the increase in compressive deformation ( $\varepsilon$ ). When the solid content increased from 3% to 11%, the fracture strength ( $\sigma_f$ ) of LG-n hydrogels increased rapidly from 7.6 to 101.2 kPa, while the fracture deformation ( $\varepsilon_f$ ) decreased gradually from 82.4 to 51.8%. The higher solid content could produce more crosslinking points in the hydrogel and form a denser network structure, which needed more energy against external pressure [45]. However, a higher solid content could enhance the  $\sigma_f$ ; excessively high solid content led to the hydrogel becoming more brittle. Therefore, to obtain the optimum comprehensive performance, the solid content of LG-n hydrogels should be maintained at a level not exceeding 11 wt%.

To further illustrate the mechanical properties of the hydrogels, the cyclic compressive test was performed to investigate their anti-fatigue performance. Taking LG-7 as a representative sample, the  $\varepsilon$  was set as 90% of the  $\varepsilon_f$ . Five successive loading–unloading tests were carried out, and the stress–strain profiles are displayed in Figure 7b. It was found that although the maximum compressive strength ( $\sigma_m$ ) exhibited a slight decrease with the increase in the cycle number, the stress recovery rates (the percentage of  $\sigma_m$  to the original value [46]) were higher than 95%. In addition, the compressive hysteresis loops almost overlapped during the five cycles, demonstrating that the hydrogels could rapidly recover their pristine shape after removing the external force [47]. The results indicated that the hydrogels possessed excellent elastic resilience and fatigue resistance.

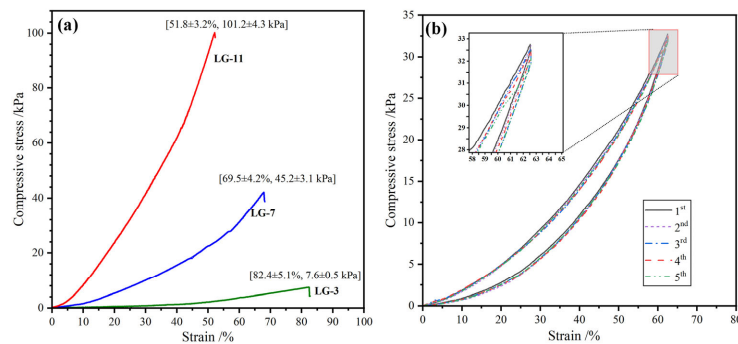


**Figure 7.** (a) Compressive stress–strain profiles of LG–n hydrogels and (b) cyclic compressive stress–strain profiles of LG–7 hydrogels.

### 2.8. Biodegradability

After serving a temporary application in the body, the medical hydrogels are expected to degrade, with degradation products being absorbable or metabolizable by the living body. In vitro degradation of the fabricated LG–n hydrogels was carried out in PBS (pH 7.4) at 37 °C using a gravimetric method, and the time-dependent mass loss is shown in Figure 8. All samples showed a rapid mass loss during the first two weeks, which was due to the dissolution of the uncrosslinked molecular chains. After degradation for 12 weeks, the mass loss for LG–3, –7, and –11 was 33.3%, 12.9%, and 8.2%, respectively. The degradation rate reduced with the increase in solid content. Higher solid content contributed to the formation of more compact crosslinked networks, which restricted the contact of water molecules with hydrolyzable amide and ester bonds, resulting in enhanced hydrolytic stability. Thus, the degradation rate of LG–n could be controlled by adjusting the solid content. It was inferred that the final hydrolytic degradation products of the hydrogels were PEG and  $\epsilon$ -lysine, which could be absorbed and metabolized by the body, respectively.

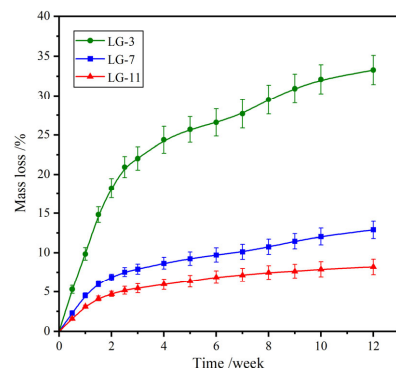


**Figure 8.** Mass loss curves of LG–n against degradation time in PBS (pH 7.4) at 37 °C ( $n = 3$ ).

### 2.9. Drug Release Performance

Ceftibuten (CFB), a third-generation cephalosporin antibiotic, is effective against a wide range of GP and GN bacteria. It is recognized for its favorable pharmacokinetic properties and remains widely used in the treatment of respiratory tract infections, otitis media, and uncomplicated urinary tract infections [48,49]. Figure 9 shows the in vitro drug release profiles of CFB from LG–n in PBS (pH 7.4) at 37 °C. Relatively high drug release rates were observed in the initial two weeks, which was the burst release of drug molecules attached to the surface of the hydrogel. After that, the rate gradually slowed down with time. Because the amide groups of CFB could form H-bonds with the amide groups of the crosslinked PEG/  $\epsilon$ -PL chain, it was difficult for drug molecules to diffuse out of the hydrogel. Hence, the drug release rate in this stage was primarily controlled by the degradation of the hydrogel. After incubation for 12 weeks, the cumulative drug release (CDR) of LG–3, –7, and –11 was 45.8%, 19.8%, and 12.9%, respectively. Therefore,

the effective drug release of LG-n was maintained for more than four months, and the fabricated hydrogels showed a prospective application for long-term drug delivery systems.

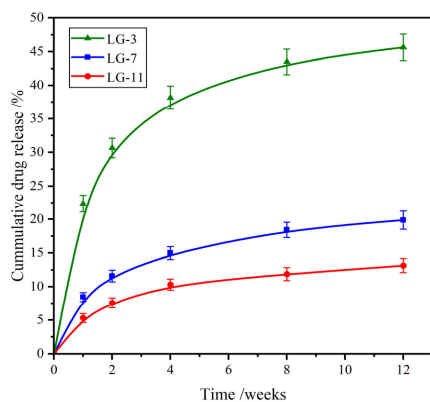


**Figure 9.** Drug release curves from LG-n hydrogels in PBS (pH 7.4) at 37 °C ( $n = 3$ ).

#### 2.10. Cytocompatibility Assay

Cytocompatibility is known as the principal step in estimating the biocompatibility of biomaterials. Here, the cell relative growth rate (RGR), survival state, and live/dead activity were adopted to assess the cytocompatibility of LG-n hydrogels with fibroblast L929 as the test cells. Figure 10 presents the RGR of cells cultured in hydrogel extracts for 72 h, as determined by the MTT assay. All the samples exhibited RGR values exceeding 95%, indicating that the solid content had minimal impact on the RGR. Based on ISO 10993–6:2007 standards [50], the cytotoxicity was class 1 and could meet the requirements for in vivo biomaterials. The optical images of cells cultured on the surface of LG-n for 72 h are displayed in Figure 11a. A large number of cells adhered to the surface of the hydrogel and presented an entirely spread morphology with elongated shapes, which manifested that the cells exhibited good survival states [51]. A cell live/dead activity test was performed on the cells cultured with LG-n extracts, and the micrographs are shown in Figure 11b. It was observed that the vast majority of cells remained viable with few dead cells. The survival status of the cells was kept consistent with the control sample. All the results confirmed that LG-n hydrogels possessed excellent cytocompatibility.

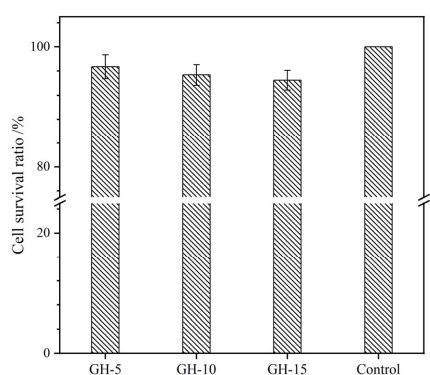


**Figure 10.** Cell survival rate in LG-n hydrogel extracts by MTT (37 °C, 72 h,  $n = 3$ ).

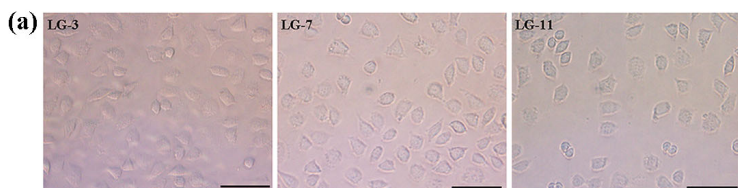


**Figure 11. Cont.**

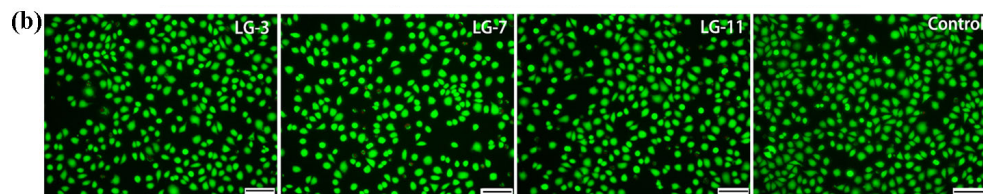


**Figure 11.** (a) Cell morphologies on LG-n hydrogel surface ( $37^{\circ}\text{C}$ , 72 h, scale bar: 100  $\mu\text{m}$ ) and (b) live/dead cells in LG-n extracts ( $37^{\circ}\text{C}$ , 72 h, scale bar: 100  $\mu\text{m}$ ).

### 2.11. Hemolysis Assay

It is difficult for medical materials to avoid contact with blood, and in vitro hemolysis testing is a simple method for evaluating their hemocompatibility in direct contact with blood [52]. The hemolysis tests were performed with anticoagulant rabbit blood, and the hemolysis rates (HRs) and hemolysis effect images for LG-n hydrogels are shown in Figure 12. The supernatant from the positive control displayed a distinct red color, which was attributed to the release of protoporphyrin from the ruptured red blood cells. In contrast, all hydrogel groups appeared transparent with a yellowish hue, which was similar to the negative control. With the HR of the positive control set at 100%, the HR values for LG-3, -7, and -11 were 2.3%, 2.5%, and 2.7%, respectively. Although the HR values exhibited a slight rise with the increase in solid content, they were all lower than 5%, demonstrating that the prepared hydrogels had a low hemolytic effect and good hemocompatibility.

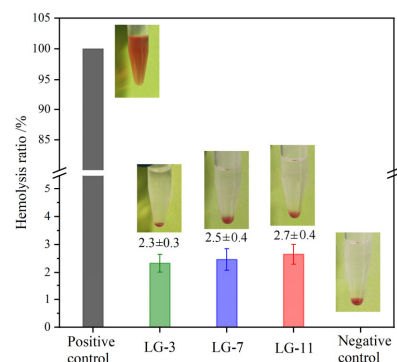


**Figure 12.** Hemolysis test images and hemolysis rates of hydrogel LG-n ( $37^{\circ}\text{C}$ , 24 h,  $n = 3$ ).

### 2.12. Antibacterial Property

During the wound-healing process, bacterial infections can lead to persistent inflammation or other complications, thus, the antibacterial capacity in biomedical hydrogels is conducive to the healing of wounds. The antibacterial activity of LG-n hydrogels against *E. coli* and *S. aureus* was measured by the inhibition zone method, and the results are presented in Figure 13. The absence of an inhibition zone in the negative control indicated no antibacterial activity. Obvious inhibition zones were formed around the LG-n, demonstrating their effectiveness in resisting the growth of *E. coli* and *S. aureus*. The antibacterial capacity increased gradually with the increase in solid content in hydrogels, which was reflected by the increased diameter of the inhibition zone from LG-3 to LG-11. The antibacterial activity was primarily attributed to the residual  $-\text{NH}_2$  of  $\epsilon$ -PL, which could interact with peptidoglycan on the bacterial cell wall [53]. Tan's groups demonstrated that  $\epsilon$ -PL could induce the structural change in peptidoglycan, which led to the destruction of the cell wall, the release of intracellular fluid, and the death of bacteria [54]. The larger inhibition zones were achieved against *E. coli* than *S. aureus*, indicating higher antibacterial activity of LG-n for GN bacteria than GP bacteria [55]. These results suggested that the broad-spectrum antibacterial LG-n hydrogels could reduce the chance of bacterial infection and showed great potential for promoting wound healing.

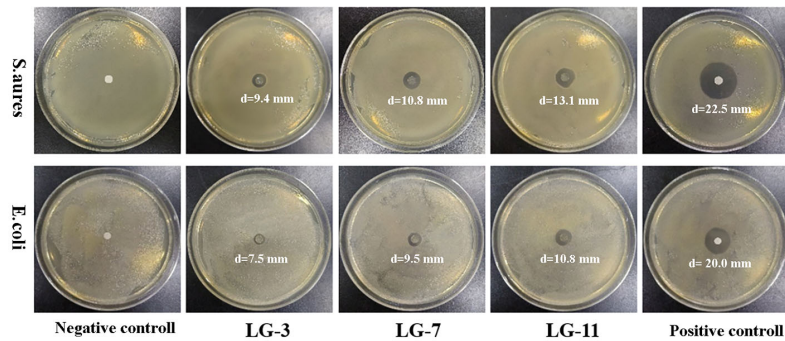


**Figure 13.** Antibacterial activities of LG-n against *E. coli* and *S. aureus*.

### 3. Materials and Methods

#### 3.1. Materials

4-Arm-PEG-OH ( $M_n = 10$  kDa) was obtained from Sigma-Aldrich (Shanghai, China) and vacuum dehydrated at 85 °C for 3.5 h before use. Glutaric anhydride (GA, 99%), 4-dimethylaminopyridine (DMAP, 95%), N-hydroxymaleimide (NHM, 97%), triethylamine (TEA, 99%), and 1-(3-dimethylaminopropyl)-3-ethylcarbodi imide (EDC, 97%) were purchased from Aladdin (Shanghai, China). ε-PL hydrochloride ( $M_n = 5.0$  kDa) was acquired from Macklin (Shanghai, China). CFB (99.5%) was supplied by Sihuan Pharmaceutical Co., Ltd. (Jinan, China). L929 Mouse fibroblasts ( $1 \times 10^6$  cells/T25) and fresh rabbit blood were acquired from Puyi Biotechnology Co., Ltd. (Shanghai, China). Other reagents were AR grade.

#### 3.2. Synthesis of 4-Arm-PEG-Mal

4-Arm-PEG-Mal was synthesized according to the reported method with slight modifications [56], as shown in Figure 14a. Briefly, 4-arm-PEG-OH (1.5 mmol), GA (18.0 mmol), and TEA (18.0 mmol) were dissolved in 150 mL of toluene. After refluxing for 24 h, the solution was concentrated to ~30 mL, which was then precipitated by diethyl ether (200 mL, −5 °C). The obtained crude product was dissolved in CH<sub>2</sub>Cl<sub>2</sub> and precipitated again with diethyl ether. After filtration and vacuum drying at room temperature, the carboxyl-terminated 4-arm-PEG (4-arm-PEG-GA) was obtained with a yield of 82.4%. 4-arm-PEG-GA (1.0 mmol) and NHM (18.5 mmol) were dissolved in 100 mL of CH<sub>2</sub>Cl<sub>2</sub>, and a CH<sub>2</sub>Cl<sub>2</sub> solution (30 mL) of EDC (18.5 mmol) was added dropwise to the system under stirring. After stirring for 24 h, the mixture was filtered, and the filtrate was concentrated to ~30 mL. The diethyl ether (200 mL, −5 °C) was added to precipitate the solution. The same purification procedure was performed twice, followed by vacuum drying at room temperature to produce 4-arm-PEG-Mal with a yield of 84.4%.

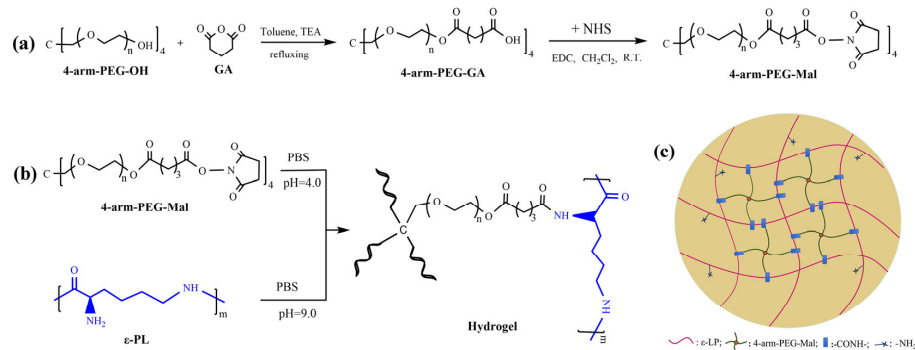


**Figure 14.** (a) Synthesis of 4-arm-PEG-Mal, (b) preparation of hydrogel LG-n, and (c) crosslinking schematic diagram of hydrogel LG-n.

The chemical structure of 4-arm-PEG-Mal was confirmed by <sup>1</sup>H NMR. <sup>1</sup>H NMR (600 MHz, CDCl<sub>3</sub>, ppm): δ 4.21 (t, –CH<sub>2</sub>–CH<sub>2</sub>–COO–), 3.80–3.44 (m, –CH<sub>2</sub>–CH<sub>2</sub>–O–), 3.38

(s, C–CH<sub>2</sub>–O), 2.84 (br, N–CO–CH<sub>2</sub>–), 2.72 (t, OOC–CH<sub>2</sub>–CH<sub>2</sub>–), 2.50 (t, –CH<sub>2</sub>–CH<sub>2</sub>–COO–N), 2.07 (m, –CH<sub>2</sub>–CH<sub>2</sub>–CH<sub>2</sub>–). Substitution degree of end groups:  $S_{\delta 2.07} : S_{\delta 3.38} = 0.93 : 1.01 = 92.1\%$ .

### 3.3. Preparation of PEG/ε-PL Hydrogels

The PEG/ε-PL hydrogels (LG-n) were crosslinked by amine/maleimide substitution reaction; the preparation process and crosslinking schematic diagram of PEG/ε-PL hydrogels are shown in Figures 14b and 14c, respectively. The molar ratio of maleimide groups to amino groups was fixed at 1:1.5. 4-Arm-PEG-Mal and ε-PL were dissolved in PBS with pH values of 4 (A solution) and 9 (B solution), respectively. The solutions were placed separately in the injection tube of a dual-chamber syringe, quickly mixed by the helical mixing head, and sprayed. The mixture was cured for ~3 min at ambient temperature to form PEG/ε-PL hydrogel, denoted as LG-n (n is the solid content of 3%, 7%, and 11%). The corresponding dry gels named DLG-n were obtained by the freeze-drying method.

### 3.4. Instruments and Characterization

The <sup>1</sup>H NMR spectrum was measured using an AVANCEII600MHz spectrometer (Bruker, Billerica, MA, USA) with CDCl<sub>3</sub> as the solvent. The FT-IR spectrum was recorded on an ALPHAII infrared spectrometer (Bruker). The dry gel was brittle-fractured in liquid nitrogen, and the cross-sectional microstructure was observed by SEM (SU-8010, Hitachi, Tokyo, Japan). The thermostability of the dry gel was determined using a TGA 2050 (Universal, New Brunswick, NJ, USA) under N<sub>2</sub> atmosphere with a heating rate of 20 °C/min. DSC 2910 (TA, New Castle, DE, USA) was adopted to measure the thermal transition, and the heating rate was set at 10 °C/min.

The swelling behavior of the hydrogel was assessed gravimetrically by measuring the mass of the absorbed water over time. The cylindrical samples (diameter: 15 mm; height: 5 mm) were weighed and immersed in deionized water at 37 °C. At a fixed time, the swollen sample was fetched out. The water on the surface was removed with filter paper and then weighed. The swelling ratio (SR) was calculated according to the formula: SR (%) = (M<sub>s</sub> – M<sub>o</sub>) / M<sub>o</sub> × 100, where M<sub>s</sub> and M<sub>o</sub> are the mass of swollen and pristine hydrogels.

The compressive stress-strain curves were obtained on cylindrical hydrogel samples (diameter: 15 mm; height: 10 mm) using a CT3 texture analyzer (Brookfield, Middleboro, MA, USA) with a TA10A probe. The compression rate was set at 0.05 mm/s and the test was conducted at room temperature.

In vitro degradability of the hydrogels was evaluated by measuring their weight-loss rate in PBS solution (pH 7.4). A wet mesh bag containing the swollen hydrogel sample was weighed (W<sub>o</sub>) and immersed in PBS. After incubation at 37 ± 0.1 °C for a determined time, the mesh bag was removed from PBS, left hanging to drain off the surface water, and weighed (W<sub>d</sub>). The degradation rate (DR) was calculated using the formula: DR(%) = (W<sub>o</sub> – W<sub>d</sub>) / W<sub>o</sub> × 100.

The drug sustained-release behavior of hydrogel was carried out according to the reported method with CFB as the model drug [57]. The drug-loaded hydrogels were prepared using the same process, except for adopting PBS solutions containing CFB (1.0 mg/mL).

The cytotoxicity assays, cell survival morphologies, and live/dead measurements were used to evaluate the cytocompatibility of the hydrogels. L929 cells served as the test cells. The cytotoxicity was performed according to the MTT method described elsewhere [58,59]. The morphology of the cells on the hydrogel surface after incubation for 72 h was observed on an inverted microscope. Calcein AM/PI staining kit (Merck, Darmstadt, Hessen, Germany) was adopted to perform the cell live/dead measurement. The cell was first cultured in hydrogel extracts for 72 h. The culture medium was subsequently sucked out, and the Calcein AM/PI staining solution was introduced. After incubation in the dark for 30 min at 5% CO<sub>2</sub> and 37 °C, the live (green, E<sub>x</sub>/E<sub>m</sub> = 494/517 nm) and dead (red, E<sub>x</sub>/E<sub>m</sub> = 535/617 nm) cells were observed under an inverted fluorescence microscope.

The hemolytic behavior of hydrogel was determined according to the requirements of GB/T 14233-2:2005 [60]. The experimental blood was collected from the hearts of healthy rabbits, and sodium citrate (5%) was added to avoid coagulation. The anticoagulated blood (8.0 mL) was diluted with normal saline (NS, 10.0 mL). The tube containing hydrogel (2.0 g) and NS (10 mL) was incubated at 37 °C for 30 min, followed by adding 0.2 mL of diluted blood and incubating for 60 min. After centrifuging for 5 min, the absorbance of the supernatant was obtained by an enzyme-linked immunosorbent assay at 540 nm. The NS and distilled water without hydrogel served as negative and positive controls, respectively. The HR was calculated according to the formula  $HR (\%) = [(A_s - A_n)/(A_w - A_n)] \times 100$ , where  $A_s$ ,  $A_n$ , and  $A_w$  were the absorbance values of the sample, negative control, and positive control, respectively.

The inhibition zone method was adopted to assess the antibacterial activity of hydrogel with Gram-negative (GN) *E. coli* and Gram-positive (GP) *S. aureus* as test bacteria. Filter papers soaked in  $\varepsilon$ -PL (5.0 mg/mL) solution and PBS solution (pH 7.4) were used as a positive and negative control, respectively. After a 24-h incubation at 37 °C, a digital camera was used to record the antibacterial effect, and the diameter of the inhibition zone was measured.

#### 4. Conclusions

This paper presents an in situ crosslinked hydrogel (LG-n) developed through the amine/maleimide reaction between 4-arm-PEG-Mal and  $\varepsilon$ -PL under physiological conditions. The effects of solid content on the physicochemical properties of the hydrogels were investigated. Although a high-solid content could increase the swelling ratio, all LG-n samples demonstrated an equilibrium swelling ratio of less than 30%. LG-7 with moderate solid content exhibited optimal compression properties with a  $\sigma_f$  of 45.2 kPa and  $\epsilon_f$  of 69.5%. Compression cycle tests revealed that LG-n exhibited good antifatigue performance. In vitro degradation studies confirmed the biodegradability of LG-n, with the degradation rate primarily governing the drug (CFB) release efficiency, resulting in a sustained-release duration of four weeks. Cytotoxicity tests, cell survival morphology observation, live/dead assays, and hemolysis tests indicated that LG-n displayed excellent cytocompatibility and low hemolytic effects (HR < 5%). Furthermore, the broad-spectrum antibacterial activity of LG-n was validated by the inhibition zone method. The biodegradable LG-n hydrogels demonstrated superior compression and antifatigue properties, excellent cytocompatibility, and favorable hemocompatibility, suggesting their promising applications in the medical field, particularly as drug sustained-release carriers and wound dressings.

**Author Contributions:** Methodology, X.D. and B.Y.; Investigation, X.D. and B.Y.; Data curation, X.D. and B.Y.; Writing—original draft, X.D.; Writing—review and editing, B.Y. and Z.H.; Funding acquisition, B.Y.; Project administration, Z.H.; Conceptualization, Z.H.; Supervision, B.Y. and Z.H. All authors have read and agreed to the published version of the manuscript.

**Funding:** This research was funded by the Shandong Provincial Social Science Planning Research Project, China, grant number 20CDCJ11.

**Institutional Review Board Statement:** Not applicable.

**Informed Consent Statement:** Not applicable.

**Data Availability Statement:** All data are contained within the manuscript and are available upon request.

**Conflicts of Interest:** The authors declare no conflicts of interest.

#### References

- Mandal, A.; Clegg, J.R.; Anselmo, A.C.; Mitragotri, S. Hydrogels in the clinic. *Bioeng. Transl. Med.* **2020**, *5*, e10158. [[CrossRef](#)] [[PubMed](#)]
- Ahmed, E.M. Hydrogel: Preparation, characterization, and applications: A review. *J. Adv. Res.* **2015**, *6*, 105–121. [[CrossRef](#)] [[PubMed](#)]

3. Thang, N.H.; Chien, T.B.; Cuong, D.X. Polymer-based hydrogels applied in drug delivery: An overview. *Gels* **2023**, *9*, 523. [[CrossRef](#)] [[PubMed](#)]
4. Dreiss, C.A. Hydrogel design strategies for drug delivery. *Curr. Opin. Colloid In.* **2020**, *48*, 1–17. [[CrossRef](#)]
5. Jose, G.; Shalumon, K.T.; Chen, J.P. Natural polymers based hydrogels for cell culture applications. *Curr. Med. Chem.* **2020**, *27*, 2734–2776. [[CrossRef](#)]
6. Yue, S.; He, H.; Li, B.; Hou, T. Hydrogel as a biomaterial for bone tissue engineering: A review. *Nanomaterials* **2020**, *10*, 1511. [[CrossRef](#)]
7. Elangwe, C.N.; Morozkina, S.N.; Olekhovich, R.O.; Polyakova, V.O.; Krasichkov, A.; Yablonskiy, P.K.; Uspenskaya, M.V. Pullulan-based hydrogels in wound healing and skin tissue engineering applications: A review. *Int. J. Mol. Sci.* **2023**, *24*, 4962. [[CrossRef](#)]
8. Khan, M.U.A.; Stojanović, G.M.; Abdullah, M.F.B.; Dolatshahi-Pirouz, A.; Marei, H.E.; Ashammakhi, N.; Hasan, A. Fundamental properties of smart hydrogels for tissue engineering applications: A review. *Int. J. Biol. Macromol.* **2024**, *254*, 127882. [[CrossRef](#)]
9. Liang, Y.; He, J.; Guo, B. Functional hydrogels as wound dressing to enhance wound healing. *ACS Nano* **2021**, *15*, 12687–12722. [[CrossRef](#)]
10. Farazin, A.; Shirazi, F.A.; Shafiei, M. Natural biomacromolecule-based antimicrobial hydrogel for rapid wound healing: A review. *Int. J. Biol. Macromol.* **2023**, *244*, 125454. [[CrossRef](#)]
11. Qi, C.; Li, A.; Wu, B.; Wang, P. Multi-sensitive Au NCs/5-FU@Carr-LA composite hydrogels for targeted multimodal anti-tumor therapy. *Molecules* **2024**, *29*, 4051. [[CrossRef](#)] [[PubMed](#)]
12. Tian, B.; Liu, J. Smart stimuli-responsive chitosan hydrogel for drug delivery: A review. *Int. J. Biol. Macromol.* **2023**, *235*, 123902. [[CrossRef](#)] [[PubMed](#)]
13. Andrade, F.; Roca-Melendres, M.M.; Durán-Lara, E.F.; Rafael, D.; Schwartz, S. Stimuli-responsive hydrogels for cancer treatment: The role of pH, light, ionic strength and magnetic field. *Cancers* **2021**, *13*, 1164. [[CrossRef](#)]
14. Kaith, B.S.; Singh, A.; Sharma, A.K.; Sud, D. Hydrogels: Synthesis, classification, properties and potential applications-a brief review. *J. Polym. Environ.* **2021**, *29*, 3827–3841. [[CrossRef](#)]
15. Liu, J.; Su, C.; Chen, Y.; Tian, S.; Lu, C.; Huang, W.; Lv, Q. Current understanding of the applications of photocrosslinked hydrogels in biomedical engineering. *Gels* **2022**, *8*, 216. [[CrossRef](#)]
16. Lin, R.Z.; Chen, Y.C.; Moreno-Luna, R.; Khademhosseini, A.; Melero-Martin, J.M. Transdermal regulation of vascular network bioengineering using a photopolymerizable methacrylated gelatin hydrogel. *Biomaterials* **2013**, *34*, 6785–6796. [[CrossRef](#)]
17. Zustiak, S.P.; Leach, J.B. Characterization of protein release from hydrolytically degradable poly(ethylene glycol) hydrogels. *Biotechnol. Bioeng.* **2015**, *108*, 197–206. [[CrossRef](#)]
18. Kim, I.; Choi, J.S.; Lee, S.; Byeon, H.J.; Lee, E.S.; Shin, B.S.; Choi, H.; Lee, K.C.; Youn, Y.S. In situ facile-forming PEG cross-linked albumin hydrogels loaded with an apoptotic TRAIL protein. *J. Control. Release* **2015**, *214*, 30–39. [[CrossRef](#)] [[PubMed](#)]
19. Ibrahim, M.; Ramadan, E.; Elsadek, N.E.; Emam, S.E.; Shimizu, T.; Ando, H.; Ishida, T. Polyethylene glycol (PEG): The nature, immunogenicity, and role in the hypersensitivity of PEGylated products. *J. Control. Release* **2022**, *351*, 215–230. [[CrossRef](#)]
20. Fu, Y.; Ding, Y.; Zhang, L.; Zhang, Y.; Liu, J.; Yu, P. Poly ethylene glycol (PEG)-related controllable and sustainable antidiabetic drug delivery systems. *Eur. J. Med. Chem.* **2021**, *217*, 113372. [[CrossRef](#)]
21. Xiao, Z.; Zhao, S.; Zhang, X.; Wei, G.; Su, Z. Recent advances in peptide engineering of PEG hydrogels: Strategies, functional regulation, and biomedical applications. *Macromol. Mater. Eng.* **2022**, *307*, 2200385. [[CrossRef](#)]
22. Gao, Y.; Joshi, M.; Zhao, Z.; Mitragotri, S. PEGylated therapeutics in the clinic. *Bioeng. Transl. Med.* **2024**, *9*, e10600. [[CrossRef](#)] [[PubMed](#)]
23. Martin, J.R.; Patil, P.; Yu, F.; Gupta, M.K.; Duvall, C.L. Enhanced stem cell retention and antioxidative protection with injectable, ROS-degradable PEG hydrogels. *Biomaterials* **2020**, *263*, 120377. [[CrossRef](#)]
24. Michel, R.; Pasche, S.; Textor, M.; Castner, D.G. Influence of PEG architecture on protein adsorption and conformation. *Langmuir* **2005**, *21*, 12327–12332. [[CrossRef](#)]
25. Fernandes-Cunha, G.M.; Chen, K.M.; Chen, F.; Le, P.; Han, J.H.; Mahajan, L.A.; Myung, D. In situ-forming collagen hydrogel crosslinked via multi-functional PEG as a matrix therapy for corneal defects. *Sci. Rep.* **2020**, *10*, 16671. [[CrossRef](#)] [[PubMed](#)]
26. Jiang, J.; Jiang, T.; Zhou, C.; He, Y.; Jiang, A.; Yang, G.; Lu, C. An adenine-modified chitosan cross-linked 8arm-PEG-CHO hydrogel for promoting infected wound healing. *Mater. Chem. Front.* **2024**, *8*, 2525–2538. [[CrossRef](#)]
27. Shih, I.L.; Shen, M.H.; Van, Y.T. Microbial synthesis of poly ( $\epsilon$ -lysine) and its various applications. *Bioresour. Technol.* **2006**, *97*, 1148–1159. [[CrossRef](#)]
28. Patil, N.A.; Kandasubramanian, B. Functionalized polylysine biomaterials for advanced medical applications: A review. *Eur. Polym. J.* **2021**, *146*, 110248. [[CrossRef](#)]
29. Chen, Y.; Miao, W.; Li, X.; Xu, Y.; Gao, H.; Zheng, B. The structure, properties, synthesis method and antimicrobial mechanism of  $\epsilon$ -polylysine with the preservative effects for aquatic products. *Trends Food. Sci. Tech.* **2023**, *139*, 104131. [[CrossRef](#)]
30. Wang, Y.; Wang, L.; Hu, Y.; Qin, J.; Yu, B. Design and optimization of  $\epsilon$ -poly-l-lysine with specific functions for diverse applications. *Int. J. Biol. Macromol.* **2024**, *262*, 129513. [[CrossRef](#)]
31. Dima, S.; Lee, Y.Y.; Watanabe, I.; Chang, W.J.; Pan, Y.H.; Teng, N.C. Antibacterial effect of the natural polymer  $\epsilon$ -polylysine against oral pathogens associated with periodontitis and caries. *Polymers* **2020**, *12*, 1218. [[CrossRef](#)] [[PubMed](#)]

32. Pourshahrestani, S.; Zeimaran, E.; Fauzi, M.B. Antibacterial polylysine- containing hydrogels for hemostatic and wound healing applications: Preparation methods, current advances and future perspectives. *Biomater. Sci.* **2024**, *12*, 3293–3320. [CrossRef] [PubMed]
33. Zhou, C.; Li, P.; Qi, X.; Sharif, A.R.M.; Poon, Y.F.; Cao, Y.; Chang, M.W.; Leong, S.S.J.; Chan-Park, M.B. A photopolymerized antimicrobial hydrogel coating derived from epsilon-poly-L-lysine. *Biomaterials* **2011**, *32*, 2704–2712. [CrossRef] [PubMed]
34. Shi, C.; Zhong, S.; Sun, Y.; Xu, L.; He, S.; Dou, Y.; Zhao, S.; Gao, Y.; Cui, X. Sonochemical preparation of folic acid-decorated reductive-responsive  $\epsilon$ -poly-L-lysine-based microcapsules for targeted drug delivery and reductive-triggered release. *Mat. Sci. Eng. C* **2020**, *106*, 110251. [CrossRef]
35. Yang, J.; Bangar, S.P.; Khan, M.R.; Hammouda, G.; Alam, P.; Zhang, W. Biopolymer-based packaging films/edible coatings functionalized with  $\epsilon$ -polylysine: New options for food preservation. *Food Res. Int.* **2024**, *187*, 114390. [CrossRef]
36. Meng, Y.; Xue, Q.; Chen, J.; Li, Y.; Shao, Z. Structure, stability, rheology, and texture properties of  $\epsilon$ -polylysine-whey protein complexes. *J. Dairy Sci.* **2022**, *105*, 3746–3757. [CrossRef] [PubMed]
37. Lang, A.; Lan, W.Q.; Xie, J. Preparation and antimicrobial mechanism of Maillard reaction products derived from  $\epsilon$ -polylysine and chitooligosaccharides. *Biochem. Biophys. Res. Co.* **2023**, *650*, 30–38. [CrossRef]
38. Hao, T.; Gao, Y.; Zheng, E.; Yang, H.; Pan, Y.; Zhang, P.; Xu, J.; Hou, Z. Multifunctional poly (ether-urethane) elastomer based on dynamic phenol-urethane and disulfide bonds: Simultaneously showing superior toughness, self-healing, shape memory, antibacterial, and antioxidative properties. *Eur. Polym. J.* **2024**, *220*, 113494. [CrossRef]
39. Zhang, Y.; Dong, Q.; Zhao, X.; Sun, Y.; Lin, X.; Zhang, X.; Wang, T.; Yang, T.; Jiang, X.; Li, J.; et al. Honeycomb-like biomimetic scaffold by functionalized antibacterial hydrogel and biodegradable porous Mg alloy for osteochondral regeneration. *Front. Bioeng. Biotechnol.* **2024**, *12*, 1417742. [CrossRef]
40. Yu, Y.; Kong, N.; Hou, Z.; Men, L.; Yang, P.; Wang, Z. Sponge-like porous polyvinyl alcohol/chitosan-based hydrogel with integrated cushioning, pH-indicating and antibacterial functions. *Inter. J. Biol. Macromol.* **2024**, *272*, 132904. [CrossRef]
41. Liao, W.; Liu, X.; Zhao, Q.; Lu, Z.; Feng, A.; Sun, X. Physicochemical, antibacterial and food preservation properties of active packaging films based on chitosan/ $\epsilon$ -polylysine-grafted bacterial cellulose. *Inter. J. Biol. Macromol.* **2023**, *253*, 127231. [CrossRef] [PubMed]
42. Yang, B.; Yin, S.; Bian, X.; Liu, C.; Liu, X.; Yan, Y.; Zhang, C.; Zhang, H.; Hou, Z. Preparation and properties of monomethoxyl polyethylene glycol grafted O-carboxymethyl chitosan for edible, fresh-keeping packaging materials. *Food. Packaging. Shelf.* **2022**, *33*, 100874. [CrossRef]
43. Lee, J.H.; Go, A.K.; Oh, S.H.; Lee, K.E.; Yuk, S.H. Tissue anti-adhesion potential of ibuprofen-loaded PLLA–PEG diblock copolymer films. *Biomaterials* **2005**, *26*, 671–678. [CrossRef]
44. Barrioni, B.R.; Carvalho, S.M.D.; Orèfice, R.L.; Oliveira, A.A.R.D.; Pereira, M.D.M. Synthesis and characterization of biodegradable polyurethane films based on HDI with hydrolyzable crosslinked bonds and a homogeneous structure for biomedical applications. *Mater. Sci. Eng. C* **2015**, *52*, 22–30. [CrossRef] [PubMed]
45. Liu, Z.; Chen, L.; Qu, L.; Zhang, R.; Qin, Z.; Zhang, H.; Wei, J.; Xu, J.; Hou, Z. Cross-linked poly(ester urethane)/starch composite films with high starch content as sustainable food-packaging materials: Influence of cross-link density. *Int. J. Biol. Macromol.* **2024**, *256*, 128441. [CrossRef] [PubMed]
46. Liu, X.; Duan, L.; Gao, G. Rapidly self-recoverable and fatigue-resistant hydrogels toughened by chemical crosslinking and hydrophobic association. *Eur. Polym. J.* **2017**, *89*, 185–194. [CrossRef]
47. Sahraro, M.; Barikani, M.; Daemi, H.; Baei, P. Anti-fatigue, highly resilient photocrosslinkable gellan gum hydrogels reinforced by flexible nanoparticulate polyurethane multi-crosslinkers. *Int. J. Biol. Macromol.* **2021**, *183*, 831–838. [CrossRef]
48. Peters, J.R.; Wells, A.D. Ceftibuten: Clinical use and effectiveness in the treatment of bacterial infections. *Int. J. Antimicrob. Ag.* **2001**, *17*, 145–152.
49. Mårlild, S.; Jodal, U.; Sandberg, T. Ceftibuten versus trimethoprim-sulfamethoxazole for oral treatment of febrile urinary tract infection in children. *Pediatr. Nephrol.* **2009**, *24*, 521–526. [CrossRef]
50. ISO 10993-6:2016; Biological Evaluation of Medical Devices. Part 6: Tests for Local Effects after Implantation. ISO: Geneva, Switzerland, 2016.
51. Hao, T.; Niu, G.; Zhang, H.; Zhu, Y.; Zhang, C.; Kong, F.; Xu, J.; Hou, Z. Enhanced hemocompatibility and antibacterial activity of biodegradable poly(ester-urethane) modified with quercetin and phosphorylcholine for durable blood-contacting applications. *J. Mater. Chem. B* **2023**, *11*, 5846. [CrossRef]
52. Zhou, H.Y.; Zhang, Y.P.; Zhang, W.F.; Chen, X.G. Biocompatibility and characteristics of injectable chitosan-based thermosensitive hydrogel for drug delivery. *Carbohyd. Polym.* **2011**, *83*, 1643–1651. [CrossRef]
53. Chen, Z.; Yao, J.; Zhao, J.; Wang, S. Injectable wound dressing based on carboxymethyl chitosan triple-network hydrogel for effective wound antibacterial and hemostasis. *Int. J. Biol. Macromol.* **2023**, *225*, 1235–1245. [CrossRef] [PubMed]
54. Tan, Z.; Shi, Y.; Xing, B.; Hou, Y.; Ciu, J.; Jia, S. The antimicrobial effects and mechanism of  $\epsilon$ -poly-lysine against *Staphylococcus aureus*. *Bioresour. Bioprocess.* **2019**, *6*, 11. [CrossRef]
55. Singh, B.; Sharma, S.; Dhiman, A. Design of antibiotic containing hydrogel wound dressings: Biomedical properties and histological study of wound healing. *Int. J. Pharmaceut.* **2013**, *457*, 82–91. [CrossRef]
56. Li, J.; Kao, W.J. Synthesis of polyethylene glycol (PEG) derivatives and PEGylated-peptide biopolymer conjugates. *Biomacromolecules* **2003**, *4*, 1055–1067. [CrossRef]

57. Hou, P.; Zhang, N.; Wu, R.; Xu, W.; Hou, Z. Photo-cross-linked biodegradable hydrogels based on n-arm-poly(ethylene glycol), poly( $\epsilon$ -caprolactone) and/or methacrylic acid for controlled drug release. *J. Biomater. Appl.* **2017**, *32*, 511–523. [[CrossRef](#)]
58. Rekha, S.; Anila, E.H. In vitro cytotoxicity studies of surface modified CaS nanoparticles on L929 cell lines using MTT assay. *Mater. Lett.* **2019**, *236*, 637–639. [[CrossRef](#)]
59. Lan, X.; Luo, T.; Zhong, Z.; Huang, D.; Liang, C.; Liu, Y.; Wang, H.; Tang, Y. Green cross-linking of gelatin/tea polyphenol/ $\epsilon$ -poly(L-lysine) electrospun nanofibrous membrane for edible and bioactive food packaging. *Food Packaging Shelf* **2022**, *34*, 100970. [[CrossRef](#)]
60. GB/T 14233-2:2005; Infusion, Transfusion, Injection Equipment for Medical Use. Part 2: Biological Test Methods. GB/T: Beijing, China, 2005.

**Disclaimer/Publisher’s Note:** The statements, opinions and data contained in all publications are solely those of the individual author(s) and contributor(s) and not of MDPI and/or the editor(s). MDPI and/or the editor(s) disclaim responsibility for any injury to people or property resulting from any ideas, methods, instructions or products referred to in the content.